

Fig. 1. A schematic representation of ADK conformational transitions. The open state (Left; PDB ID: 2RH5) is in the apo state. The closed state (Right; PDB ID: 2RGX) is bound to Ap5A nucleotide. The semiopen state (Upper; PDB ID: 2AK3) is in complex with AMP, and its AMP lid is in a closed conformation. The other semiopen state (Lower; PDB ID: 1DVR) is in complex with an ATP analog (phosphodifluoromethylphosphonic acid-adenylate ester), and its ATP lid is in a closed conformation.

(PDB) ID: 2RH5 chain A] and closed (PDB ID: 2RGX) conformations (14). Tests with the open and closed structures of *Escherichia coli* ADK gave similar results.

We first performed transition calculations using a control algorithm with a simple harmonic potential. Then, hoping to reduce geometric distortions, we used that same algorithm with a harmonic potential modified to include restraints on the virtual $C\alpha$ - $C\alpha$ bonds. Finally, we devised the VAMM approach, which adds other restraints to give a complete potential function for virtual atoms, improves the algorithm for transition pathway calculations, and also includes periodic energy minimizations and periodic reassessments of secondary structure as needed for the VAMM force field.

Convergence of ADK Transition Pathway Intermediates. Transition pathway calculations converged slowly for the control algorithm, as seen in the progression of rmsd between the alternative intermediates generated from initial open and closed structures of ADK (Fig. 2 and Fig. S1). These deviations dropped from an rmsd of 5.85 Å initially to 1.5 Å in 637 and 699 iterations for the simple harmonic and bond-restrained potentials, respectively; however, convergence beyond this point was very inefficient. To reach 1 Å rmsd required 7,655 total steps with only bond restraints, and the system stalled at ≈ 1.1 Å rmsd with the simple harmonic potential and was discontinued after 7,500 iterations. This situation indicates a very ineffective algorithm.

On the other hand, the VAMM algorithm yielded a transition pathway that converged strikingly fast, requiring only 178 steps to reach 1 Å rmsd (Fig. 2B). As moves proceeded toward convergence, the involvement coefficients of engaged normal modes decreased,

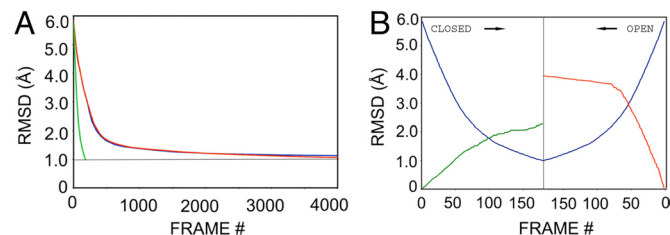


Fig. 2. Structural deviations along ADK transition pathways. (A) Deviations (rmsd) between the succession of two intermediate states generated from open and closed ADK, respectively, as analyzed with the simple harmonic potential (blue), with the bond-restrained potential (red), and with the VAMM potential (green). (B) Deviations during the VAMM-based transition calculations. An expanded view is shown for deviations (rmsd) between the succession of VAMM intermediate states as they move, frame by frame, from the respective closed (Left) and open (Right) states toward similar terminal intermediates (blue). Deviations between the closed state and intermediates generated from the closed state (green) and deviations between the open state and intermediates generated from the open state (red) are also shown.

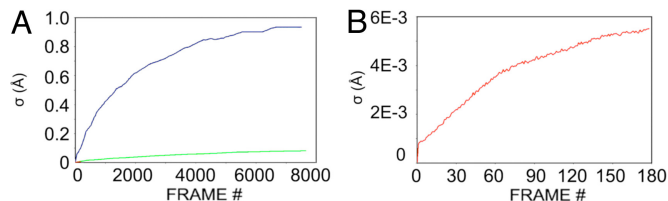


Fig. 3. SDs (σ) of $C\alpha$ - $C\alpha$ virtual bonds during trajectories starting from the open state of ADK (rmsd between intermediate- and starting-state distances). (A) Comparison of trajectories based on different potential functions: simple harmonic potential (blue), bond-restrained harmonic potential (green), and VAMM potential (red). (B) VAMM-based trajectory in an expanded view.

and the frequencies of these modes tended to increase (Fig. S2). The increased efficiency of the VAMM algorithm, reflecting the more comprehensive energetic restraints, also implies lowered computational strain along the transition pathway and structurally more realistic intermediates. Intermediates generated from the open state deviated from the initial structure more than those generated from the closed state. For VAMM, the rmsd between the open-state crystal structure and its terminal intermediate was 3.94 Å, whereas that between the closed-state crystal structure and its terminal intermediate was only 2.26 Å (Fig. 2B). This result is in accord with FRET experiments (9), which indicate that the unliganded, open state samples a much larger conformational space.

Accuracy of Calculated $C\alpha$ - $C\alpha$ Virtual Bond Lengths. Distances between adjacent $C\alpha$ atoms are strictly confined to the vicinity of 3.8 Å for *trans*-peptide bonds of the protein molecules. We find that the distribution of the $C\alpha$ - $C\alpha$ bonds in the EVA database (20) has a 3.78-Å mean value and an SD (σ) of 0.0093 Å; $C\alpha$ - $C\alpha$ distances below 3.45 Å and above 4.15 Å are almost never observed, and even the next nearest values (in the range of 3.45–3.65 Å and 3.95–4.15 Å) are very rare, with $p[3.45,3.65] = 6.3 \times 10^{-3}$ and $p[3.95,4.15] = 3.6 \times 10^{-4}$. Thus, even minor deviations from the equilibrium values are not usually allowed for $C\alpha$ - $C\alpha$ virtual bond distances.

In violation of this reality, the SDs of $C\alpha$ - $C\alpha$ distances along transition pathways (Fig. 2A) reveal gross distortions for the simple harmonic potential (terminal $\sigma = 0.93$ Å) and even unacceptable departures for the bond-restrained potential (terminal $\sigma = 0.08$ Å). Many distances fell into the highly disallowed range for *trans*-peptides ($3.5 \text{ \AA} < d < 4.1 \text{ \AA}$), with maximum distances of 7.21 Å and 4.03 Å for simple and bond-restrained potentials, respectively. Iterative fitting of normal modes computed by using simple harmonic potentials clearly generates unrealistic bond distances.

In sharp contrast with the control algorithms, the $C\alpha$ - $C\alpha$ distances from the VAMM algorithm conformed to standard values throughout the transition (Fig. 3C). The terminal intermediate state originated from the open ADK had $\sigma = 0.0055$ Å, in the same range as that deduced from the entire EVA database. All of the virtual *trans*-bond distances fell within the range between 3.7 Å and 3.9 Å. Thus, VAMM provides an accurate tool for preserving the integrity of virtual bond distances during a pathway calculation.

Accuracy of Virtual Bond and Dihedral Angles. Protein conformations are well defined by their backbone (φ, ψ) dihedral angles, and distributions of polypeptide conformations in accurate crystal structures allow for the definition of probability contours in familiar Ramachandran (φ, ψ) plots (21). Although (φ, ψ) angles are not defined in $C\alpha$ virtual-atom representations of proteins, a comparable picture of the conformational state is specified by the virtual $C\alpha$ - $C\alpha$ - $C\alpha$ bond angles τ and the virtual $C\alpha$ - $C\alpha$ - $C\alpha$ - $C\alpha$ dihedral angles θ . Distributions of (τ, θ) pairs are plotted in Fig. 4A–E for the open-state crystal structure and terminal intermediate states generated from it. Probability contours deduced from the Top500 database (21) are drawn at the MolProbity levels of 95% (favored)

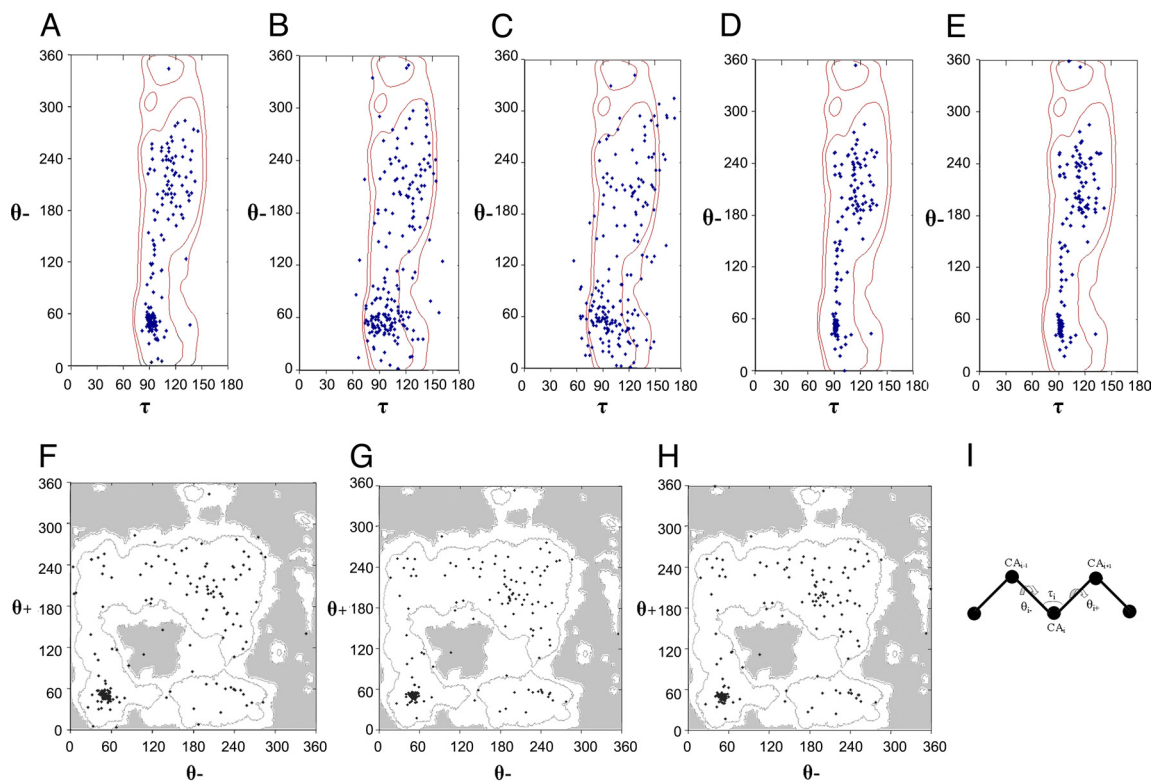


Fig. 4. Distributions of virtually bonded conformation parameters. Conformational values from defined ADK structures are spotted (blue dots) onto contour plots based on the MolProbity Top500 database (21). (A–E) θ^- vs. τ profile. Contour levels are at 95% (favored) and 99% (allowed). (A) Crystal structure of open ADK. (B) The terminal intermediate state generated from open ADK using the simple harmonic control algorithm. (C) The terminal intermediate state generated from open ADK using the bond-restrained control algorithm. (D) The open ADK structure after energy minimization with VAMM. (E) The terminal intermediate state generated from open ADK using the VAMM-potential algorithm. (F–H) The θ^- vs. θ^+ profile. Contour levels are at 95% (favored) and 99% (allowed). (F) Crystal structure of open ADK. (G) The open ADK structure after energy minimization with VAMM. (H) The terminal intermediate state generated from open ADK using the VAMM algorithm. (I) Definition of virtual bond (τ) and virtual dihedral (θ) angles.

and 99% (allowed). Similar distributions of virtual bond and dihedral angles were reported previously (22).

For the crystal structure of open ADK, no outlier (>99%) was observed (Fig. 4A), and only two residues were outside the favored (>95%) region (Table S1). The virtual dihedral angle vs. bond angle plots for the VAMM-minimized open ADK structure (Fig. 4D) and for the open-state terminal intermediate state calculated by the VAMM algorithm (Fig. 4E) were both similar to the experimental result, with no outliers for either and only one residue for each outside the favored region.

In contrast to VAMM, intermediate states generated by using the control algorithms contained several outlier residues [nine from the simple harmonic model (Fig. 4B), and 24 from the bond-restrained model (Fig. 4C)]. Interestingly, restraining the virtual bond distances caused more unrealistic curvilinear distortions in ADK as a payoff for the more realistic $C\alpha-C\alpha$ distances (Fig. 3A). Pathway calculations based on simple harmonic potentials clearly yielded distorted molecules.

The distributions of virtual bond angles in (τ, θ) pairs from VAMM-based structures conform statistically with observations from the PDB (Fig. 4), which further validates VAMM as being sufficient to calculate intermediate states that are in accordance with the physical laws imposed on macromolecules. Moreover, because outliers occur frequently when simple harmonic potentials are used, we conclude that VAMM has a clear superiority in pathway calculations.

Distributions of Neighboring Dihedral Angles. The analysis of virtual bond and dihedral angle distribution plots reveals that allowed virtual bond angles were confined to the interval 80° to 150°,

whereas allowed dihedral angles spanned the entire range, from 0° to 360° (Fig. 4A–E). Thus, an alternative approach is needed to analyze accuracy of the virtual dihedral angles. Here, we analyze distributions of the consecutive virtual dihedral angles preceding (θ^-) and following (θ^+) a given $C\alpha$ atom, again deriving probability contours from the Top500 database. Values for open ADK were spotted on contoured θ^- vs. θ^+ plots (Fig. 4F–H).

The θ^-/θ^+ plot from the open-state ADK crystal structure conformed well to the contours of allowance (Fig. 4F), but there were three outlier residues. These outlier dihedrals all joined central glycine residues, however, indicating a greater dihedral liberty at glycine positions, as is also seen in Ramachandran plots. The number of outliers dropped to two in the θ^-/θ^+ plot from the minimized open structure (Fig. 4G) and to one in the plot from the terminal intermediate state (Fig. 4H), both of which derived from VAMM. The θ^-/θ^+ plots from control-based structures showed 14 outliers (i.e., outside the 99% probability level) from the simple harmonic model, and 15 outliers from the bond-restrained potential (Table S1). Here again, we see that VAMM maintains structural integrity, in keeping with a realistic transition pathway, whereas unrealistic distortions are encountered in calculations from simple potentials.

Strain Energy of ADK Intermediates. The strain energy of intermediate structures from ADK transitions was calculated with a double-well potential (see Methods). This strain energy is a measure of deviation from native contacts that exist in the initial input structures. Computational strains are shown for transition pathways based on each of the potential function algorithms (Fig. 5).

The comparison shows that the VAMM-based conformational

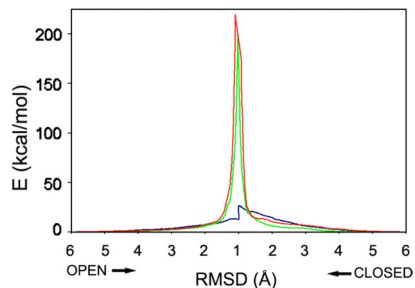


Fig. 5. Energetics of ADK transitions. The strain energies stored in intermediate states are shown for trajectories computed with the simple harmonic (red), bond-restrained (green), and VAMM (blue) potentials. In each case, the strain energies in trajectories from both the open and the closed states are plotted against rmsd values between intermediates as they approach one another, ultimately reaching terminal intermediates.

transition generated significantly less computational strain (maximal strain energy of 26.6 kcal/mol) than happened with the control algorithms (up to 219.1 kcal/mol and 199.5 kcal/mol from the simple harmonic and bond-restrained approaches, respectively). Values from harmonic potentials were in the same high range as those found with other coarse-grained approaches using similar potentials (17, 18). Thus, the VAMM algorithm significantly decreases the energy barrier for transition pathways, which is in accord with the more realistic geometric features and the greater efficiency of the method.

In summary, all of our tests validate the performance of the VAMM algorithm, and we describe results of our applications to ADK based entirely on VAMM computations.

Application Results

Conformational Transition Pathways in ADK. Differences between fully open (no ligand) and closed (Mg^{2+} , Ap5A) states of ADK (9) are accounted for almost entirely by rigid hinge-bending rotations of the ATP-lid domain (χ_1) and the AMP-lid domain (χ_2) relative to the core domain, which we measured here relative to their dispositions in the closed state. By using program TOSS (23), we found that rotations of ($\chi_1 = 38.1^\circ$, $\chi_2 = 35.2^\circ$) superimpose the two lid domains from the open-state crystal structure onto those of the closed state, and thereby reduce the rmsd from 5.85 Å to 1.40 Å. The two terminal intermediates from the VAMM algorithm have very similar lid conformations ($\chi_1 = 21.6^\circ$, $\chi_2 = 10.6^\circ$) vs. ($\chi_1 = 19.4^\circ$, $\chi_2 = 6.1^\circ$), as generated from the open and closed states,

respectively, and the terminal rmsd (1 Å) is even less than that from direct rigid-body superposition (1.40 Å).

The conformational transition between open and closed states of ADK is constructed as the joining of two trajectory segments, closure computed from a fully open state and opening from a fully closed state. We used the two lid-domain angles (χ_1 and χ_2) to monitor evolution of the trajectory and, because the terminal intermediates meeting from opposite directions are so similar, we invoked reversibility to reconstruct the entire transition from closed to open or vice versa (Fig. 6A). Closure from the open state proceeded quickly to reach (χ_1 , χ_2) of (27.4° , 25.3°) after only 60 steps on way to the terminal intermediate (21.6° , 10.6°) at 178 steps. Further closure of the ATP lid (χ_1) proceeded more slowly, but the AMP lid (χ_2) closure continued at the same pace. Opening from the closed state proceeded sharply for the AMP lid (χ_2) for a few steps and then meandered slowly toward the terminal intermediate, whereas the ATP lid (χ_1) opened more smoothly over the course of ≈ 100 steps to (15.7° , 5.3°) before ultimately reaching the terminal intermediate (19.4° , 6.1°) at 178 steps. The juncture between forward and reverse directions was relatively smooth (Fig. 6A and B).

The computed transition pathway can be visualized in an animation of the course for closing from the open state through the terminal intermediate states to complete closure by reversal of opening from the closed state (Movie S1). This trajectory shows a very large rearrangement of the open state to a semiclosed form during the initial stages. This is consistent with the FRET experiments that showed the rapid partial closure of the open state (9). After the semiclosed state formed, the transition slowed down and did not sample a large space around this semiclosed form. The closed state sampled a narrower portion of the conformational space, with a limited opening of the ATP- and AMP-lid domains.

Comparison with Crystallographic Intermediate States. We studied trajectories that targeted only one or the other lid domain as well as that for the entire ADK molecule. The couplings of χ_1 and χ_2 angles during these conformational transitions of ADK are shown in Fig. 6B together with the locations of intermediate ADK crystal structures in the (χ_1 , χ_2) space. The trajectories, viewed from open (Fig. 6B Upper Right) to closed (Fig. 6B Lower Left) states, can be thought to mimic the binding of Ap5A (Fig. 6B, blue curve) and, in some sense, of ATP (Fig. 6B, red curve) and AMP (Fig. 6B, green curve). The entire structure was included in the transition pathway calculation for the blue curve, but the AMP-lid domain was excluded from calculations of involvement coefficients for the red curve, and the ATP-lid domain was excluded for the green curve.

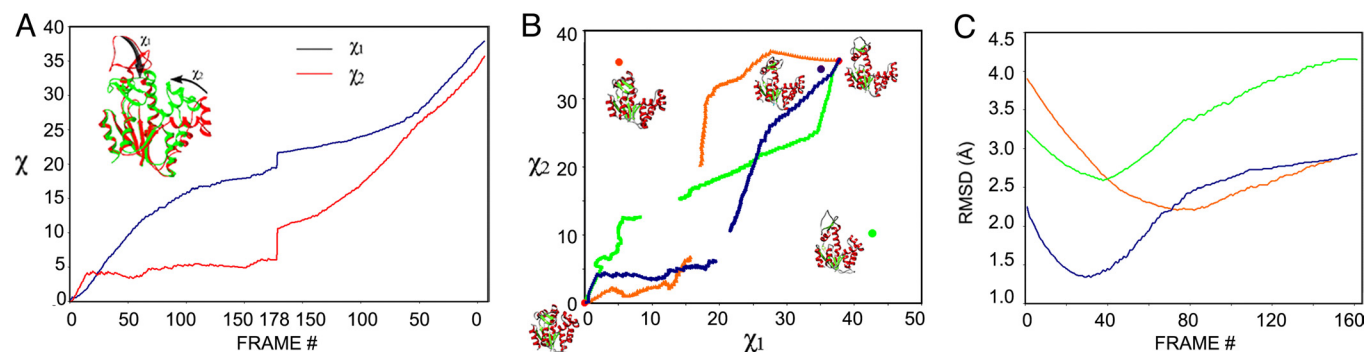


Fig. 6. The conformational transition of ADK. (A) The evolution of χ angles along the progression of ADK trajectories from closed (Left) and open (Right) states toward similar terminal intermediates (Middle). (B) The coupling of χ_1 and χ_2 . The conformations of intermediate crystal structures are shown on the χ_1 , χ_2 domain angle space alongside dots at respective χ_1 , χ_2 , color-coded corresponding to C. Trajectories are plotted starting from closed-state ADK (Left) and open-state ADK (Right): entire structure involved in targeting (blue), AMP-lid domain excluded from targeting (red), and ATP-lid domain excluded from targeting (green). (C) Deviations (rmsd) between the trajectory intermediate states and respective intermediate crystal structures: semiclosed apo state (PDB ID: 2RH5) vs. the fully targeted trajectory (blue); complex with ATP analog AMPPCF₂P (PDB ID: 1DVR) vs. the ATP-lid-directed trajectory (orange); and complex with AMP (PDB ID: 2AK3) vs. the AMP-lid-directed trajectory (green).

Such domain-selected calculations can be used for dissecting potential allosteric couplings; based on our calculations, the two closures in ADK are relatively uncoupled.

When both lid domains were targeted, ADK followed an initial trajectory roughly diagonal in the (χ_1, χ_2) space. It passed at $(\chi_1 = 36.1^\circ, \chi_2 = 33.3^\circ)$, very close to values $(\chi_1 = 35.1^\circ, \chi_2 = 34.3^\circ)$ of a semiclosed structure (PDB ID: 2RH5, chain C), which has been shown to lie on the trajectory of ADK closure (9). When only the core and ATP-lid domains were targeted, as in a trajectory that might be induced by binding of an ATP analog (7), intermediate states approached $(\chi_1 = 18.2^\circ, \chi_2 = 30.2^\circ)$, the conformation $(\chi_1 = 5.1^\circ, \chi_2 = 35.4^\circ)$ of an ATP-lid closed/AMP-lid open crystal structure (PDB ID: 1DVR). When only the core and AMP-binding domains were targeted, intermediate states approached $(\chi_1 = 34.1^\circ, \chi_2 = 25.0^\circ)$ the conformation $(\chi_1 = 42.8^\circ, \chi_2 = 10.3^\circ)$ of the crystal structure (PDB ID: 2AK3) of an AMP complex (24).

Deviations of computed trajectory intermediates from crystal structures of intermediate states are consistent with the preceding (χ_1, χ_2) plot analysis. Minima close to experimental intermediates occurred in each of the respective rmsd plots against intermediate crystal structures (Fig. 6C). The closest approaches of trajectory intermediates to the observed crystal structures were at 1.34 Å rmsd for the semiclosed apo state (Fig. 6C, blue), 2.21 Å rmsd for the ATP analog complex (Fig. 6C, orange), and 2.59 Å for the AMP complex (Fig. 6C, green). The red and green domain-selected trajectories are biased toward the respective ATP and AMP complex structures, but their more distant close approaches may reflect either coupling between the lid domains or calculation defects.

Discussion

In all respects, the VAMM force field with its associated algorithm for iterative fitting of normal modes and energy minimization is superior in conformational transition calculations to algorithms based on simple harmonic potentials. This is not to diminish that elastic network models are highly effective for analyzing motions near the native state. First, transition pathway calculations are significantly more efficient with the VAMM-based algorithm. Second, with simple potentials, the $C\alpha$ – $C\alpha$ bond distances show absurd deviations from their equilibrium states, whereas the VAMM preserves the virtual $C\alpha$ – $C\alpha$ bond integrity. Third, the VAMM-based algorithm generates accurate virtual bond and dihedral angles compared with the simple network models. Fourth, the VAMM-based algorithm generates a transition trajectory with significantly lower computational strain.

Several computational and experimental studies of protein dynamics show that proteins in an unbound state can fluctuate with varying populations over an ensemble of conformations that sample states adopted in complexes with ligands or binding partners (25–27). The conformational space accessible to an uncomplexed apo state is likely to be greater than that accessible in a state closed down onto a ligand. The transition pathways found here for ADK are consistent with this view. In our calculations, ADK moves quite freely and rapidly away from the open state but more slowly and with greater restriction away from the closed state (Figs. 2B and 6A). Indeed, the most populated subspaces may not necessarily lie on the most likely trajectory. Relaxed states that approach the “closed-state ensemble” defined by the restricted fluctuations about the closed state dictate the most likely conformational trajectory. In our current description of the ADK system, slight openings of the ATP- and AMP-lid domains are followed by further opening of the ATP-lid domain within the narrow conformational space of the closed system. Open states that can adapt to this confine are selected to drive the full conformational transition. A more realistic description of such conformational transitions will require inclusion of stochastic processes in the algorithm to yield an ensemble of transition pathways populated around the most likely pathway.

The VAMM algorithm for conformational transition pathway calculations is very versatile and not restricted by ADK-specific characteristics. Because of its coarse-grained nature, it is not limited by protein size; because it uses iterative normal-mode fittings rather than simulations requiring short integration time intervals, it is not limited by the amplitude or time scale of the conformational change. Moreover, because the VAMM potential is completely general, the algorithm is not limited to hinge-bending motions. It is directly applicable as well to shear motions, as in citrate synthase (28), or more complicated conformational changes such as in HIV envelope glycoprotein gp120. Being coarse-grained, VAMM necessarily has limitations; for example, there is insufficient detail for calculation of energetic barriers. Nevertheless, we expect that the VAMM algorithm for conformational transition calculations will be useful quite generally in describing large conformational transitions in even the largest of protein complexes.

Methods

Potential Functions. We have performed parallel calculations based on three different coarse-grained potential functions.

A simple harmonic potential function, which models all interactions between residues within a cutoff radius (13 Å) as springs to calculate a subset of the slow normal modes (29), serves as a control. It is given by

$$V_{\text{harmonic}} = \sum_{i,j}^N k \times (|\vec{R}_{i,j}| - |\vec{R}_{i,j}^0|)^2. \quad [1]$$

A uniform spring constant k of value 1 kcal/molÅ² is adopted for all residues that are closer than the cutoff distance. \vec{R}_{ij} represents the displacement vector, and R_{ij}^0 represents the equilibrium distances between positions of $C\alpha$ atoms i and j . N is the number of residues.

An alternative approach is taken to introduce additional restraints to the neighboring $C\alpha$ atoms to model pseudo bonds between each residue. The modified potential becomes

$$V_{\text{Bond-restrained}} = \sum_i^N k_{\text{bond}} \times (|\vec{R}_{i,i+1}| - |\vec{R}_{i,i+1}^0|)^2 + \sum_{i,j}^N k_{\text{nonbond}} \times (|\vec{R}_{i,j}| - |\vec{R}_{i,j}^0|)^2. \quad [2]$$

In this bond-restrained model, k_{bond} is the spring constant of the interaction between neighbor $C\alpha$ atoms, and k_{nonbond} is the spring constant of the interaction between nonbonded neighbor $C\alpha$ atoms. A value of 70 kcal/molÅ² is adopted for k_{bond} based on the statistical analysis and Boltzmann inversion of the crystallographic data.

The fully elaborated VAMM force field is

$$V_{\text{VAMM}} = V_{\text{bonded}} + V_{\text{angle}} + V_{\text{dihedral}} + V_{\text{nonbonded}} + V_{\text{local}} \quad [3]$$

where each of the terms is defined in a companion paper (19). In brief, V_{bonded} is the same bond-restraint term as for $V_{\text{Bond-restrained}}$ in Eq. 2, including separate definitions for *trans*- and *cis*-peptide bonds and for disulfide bonds; V_{angle} is for restraints on virtual bond angles τ , which depend on type of secondary structure; V_{dihedral} is for restraints on virtual dihedral angles θ , which also depend on secondary structure; $V_{\text{nonbonded}}$ is for restraints on nonbonded interactions between atom pairs more than five residues apart, which are specific to amino acid identities; and V_{local} is for restraints that maintain local geometries.

Iterative Normal-Mode-Driven Transitions. We computed the transition pathway between two alternative conformations, A (e.g., open-state ADK) and B (e.g., closed-state ADK), by moving each structure toward the other in iterations of moves directed at each step along the normal mode of greatest engagement with its target structure. Only protein residues are modeled; bound ligands are implicit. For each structure, from the starting points at A_0 and B_0 through intermediates A_i and B_i at each step i , the Hessian matrix is constructed from the particular potential function used in that analysis (Eq. 1, 2, or 3) and diagonalized to compute normal modes (30, 31).

In general, 20 slow modes are considered sufficient to span the slow fluctuations of macromolecules that sample the functional motions (17). Thus, we

screened the 20 lowest-frequency normal modes for each of conformations A_i and B_i to find that normal mode from each vibrating state having the greatest Marques-Sanejouand overlap factor (32) with the alternate, target state. This factor, also called the involvement coefficient by Ma and Karplus (33), measures how much a given normal mode contributes to the molecular displacement between two conformers. The involvement coefficient, I_{ik} , is the projection of the normal-mode vector onto the linear displacement:

$$I_{ik} = \frac{\left| \sum_{j=1,3N} \vec{L}_{kj} \cdot \Delta \vec{R}_j \right|}{\left[\sum_{j=1,3N} L_{kj}^2 \cdot \sum_{j=1,3N} \Delta R_j^2 \right]^{1/2}} \quad [4]$$

where at step i , L_{kj} is the component from eigenvector k acting on atom j , and ΔR_j is the displacement vector between the intermediate states generated from alternative starting structures. Both for the mode from A_i with highest involvement coefficient into the direction of B_i and for the mode of B_i with highest involvement coefficient into the direction A_i , each direction of the mode must be tested, which we do by calculating the pairwise rmsd values between four possible conformers generated from states A_i and B_i after applying shifts dictated by the respective modes in each of the alternative directions.

The shifts for each move for residue j are found by

$$\Delta \vec{X}_{jk} = \pm C \cdot \sqrt{\frac{N}{3N} \cdot \vec{L}_{jk}} \cdot \vec{L}_{jk} \quad [5]$$

$$\sqrt{\lambda_k \sum_j (\vec{L}_{jk})^2}$$

where C is a constant chosen as 0.005, λ_k is the eigenvalue of mode k , L_{jk} is the eigenvector for mode k acting at atom j , and \pm refers to the alternative directions for this mode. Tests showed that the nature of conformational transitions is relatively insensitive to the value of C within a certain interval (Table S2), and 0.005 was chosen so that the calculations are performed within a feasible CPU time and without unrealistic distortions due to large step sizes.

The two new conformers from shift sets giving minimal rmsd values then become the input structures for the next iteration step. The process continues until intermediate conformers A_i and B_i converge to within the convergence criteria, which is usually set as an rmsd value of 1 Å. This cutoff value is appropriate because the normal modes calculated from two structures that are closer than 1 Å rmsd are not significantly different (34), and two such structures are generally

very similar, except at flexible loops. A more lenient criterion might be set in cases where complicated motions, such as in flexible loops or local folding events, are also involved in contrast to the transition observed in ADK.

Control Algorithm. Computations of conformational transitions with the simple harmonic potential (Eq. 1) or the bond-restrained harmonic potential (Eq. 2) use the algorithm shown in Fig. S3. Normal modes and iterative moves are made as described above, sampling the 20 lowest-frequency modes and moving in the direction of normal modes having greatest involvement in the directions toward the respective target structures.

VAMM Algorithm. Computations of conformational transitional pathways with the VAMM potential function (Eq. 3) use the algorithm shown in Fig. S4. The VAMM algorithm is similar to the control algorithm, but additional requirements are imposed. In the initial step, secondary structures needed for VAMM are assigned from the crystal structure coordinates of conformers A_0 and B_0 by using the DSSP algorithm (35). This step is followed by a truncated Newton minimization of the $C\alpha$ system in the VAMM force field to a gradient of 0.1 kcal/molÅ (36). Hessian matrices are constructed from each of these minimized structures by using VAMM and are then diagonalized for normal-mode evaluations. The procedure is iterated as described above to generate successive intermediates A_i and B_i . As the calculation proceeds, secondary structures of the computed intermediate states are updated at intervals of 0.1 rmsd (rmsd_{UPDATE}) between the calculated intermediate states. The rmsd_{UPDATE} values between 0.1 and 0.5 Å generated reliable and consistent results on calculation of the ADK transition. In addition, energy minimizations of the intermediate states are performed whenever the energy gradient rises above 1 kcal/molÅ. This approach keeps the system near-local energy minima and also helps to relax artificially high strains. The convergence criterion is again 1 Å rmsd.

Distributions of Virtually Bonded Conformation Parameters. Probability contour plots for relevant conformational parameters were evaluated from the same Top500 database (21) as used to produce Ramachandran plots by the MolProbity software (37). Details are in *SI Text*.

Strain Energy of Intermediate States. Strains that accumulate during conformational transitions are calculated with a double-well potential similar to that for the plastic network model (18). Details are in *SI Text*.

ACKNOWLEDGMENTS. We thank Barry Honig for comments on the manuscript. This work was supported in part by National Institutes of Health Grant GM56550 (to W.A.H.).

- Kern D, Zuiderweg ERP (2003) The role of dynamics in allosteric regulation. *Curr Opin Struct Biol* 13:748–757.
- Yon JM, Perahia D, Ghelis C (1998) Conformational dynamics and enzyme activity. *Biochimie* 80:33–42.
- Adcock SA, McCammon JA (2006) Molecular dynamics: Survey of methods for simulating the activity of proteins. *Chem Rev* 106:1589–1615.
- Bahar I, Rader AJ (2005) Coarse-grained normal mode analysis in structural biology. *Curr Opin Struct Biol* 15:586–592.
- Vonrhein C, Schlauderer GJ, Schulz GE (1995) Movie of the structural changes during a catalytic cycle of nucleoside monophosphate kinases. *Structure* 3:483–490.
- Muller CW, Schlauderer GJ, Reinstein J, Schulz GE (1996) Adenylate kinase motions during catalysis: An energetic counterweight balancing substrate binding. *Structure* 4:147–156.
- Schlauderer GJ, Proba K, Schulz GE (1996) Structure of a mutant adenylate kinase ligated with an ATP-analogue showing domain closure over ATP. *J Mol Biol* 256:223–227.
- Schlauderer GJ, Schulz GE (1996) The structure of bovine mitochondrial adenylate kinase: Comparison with isoenzymes in other compartments. *Protein Sci* 5:434–441.
- Henzler-Wildman KA, et al. (2007) Intrinsic motions along an enzymatic reaction trajectory. *Nature* 450:838–844.
- Hanson JA, et al. (2007) Illuminating the mechanistic roles of enzyme conformational dynamics. *Proc Natl Acad Sci USA* 104:18055–18060.
- Arora K, Brooks CL (2007) Large-scale allosteric conformational transitions of adenylate kinase appear to involve a population-shift mechanism. *Proc Natl Acad Sci USA* 104:18496–18501.
- Snow C, Qi GY, Hayward S (2007) Essential dynamics sampling study of adenylate kinase: Comparison to citrate synthase and implication for the hinge and shear mechanisms of domain motions. *Proteins* 67:325–337.
- Kubitzki MB, de Groot BL (2008) The atomistic mechanism of conformational transition in adenylate kinase: A TEE-REX molecular dynamics study. *Structure* 16:1175–1182.
- Henzler-Wildman KA, et al. (2007) A hierarchy of timescales in protein dynamics is linked to enzyme catalysis. *Nature* 450:913–916.
- Whitford PC, Miyashita O, Levy Y, Onuchic JN (2007) Conformational transitions of adenylate kinase: Switching by cracking. *J Mol Biol* 366:1661–1671.
- Zheng WJ, Brooks BR, Hummer G (2007) Protein conformational transitions explored by mixed elastic network models. *Proteins* 69:43–57.
- Kirilova S, Cortes J, Stefaniou A, Simeon T (2008) An NMA-guided path planning approach for computing large-amplitude conformational changes in proteins. *Proteins* 70:131–143.
- Maragakis P, Karplus M (2005) Large amplitude conformational change in proteins explored with a plastic network model: Adenylate kinase. *J Mol Biol* 352:807–822.
- Korkut A, Hendrickson WA (2009) A force field for virtual atom molecular mechanics of proteins. *Proc Natl Acad Sci USA* 106:15667–15672.
- Eyrich VA, et al. (2001) EVA: Continuous automatic evaluation of protein structure prediction servers. *Bioinformatics* 17:1242–1243.
- Lovell SC, et al. (2003) Structure validation by C alpha geometry: Phi, psi and C-beta deviation. *Proteins* 50:437–450.
- Bahar I, Kaplan M, Jernigan RL (1997) Short-range conformational energies, secondary structure propensities, and recognition of correct sequence-structure matches. *Proteins* 29:292–308.
- Hendrickson WA (1979) Transformations to optimize the superposition of similar structures. *Acta Crystallogr A* 35:158–163.
- Diederichs K, Schulz GE (1991) The refined structure of the complex between adenylate kinase from beef-heart mitochondrial matrix and its substrate AMP at 1.85 Å resolution. *J Mol Biol* 217:541–549.
- Eisenmesser EZ, et al. (2005) Intrinsic dynamics of an enzyme underlies catalysis. *Nature* 438:117–121.
- Bahar I, Chennubhotla C, Tobi D (2007) Intrinsic dynamics of enzymes in the unbound state and, relation to allosteric regulation. *Curr Opin Struct Biol* 17:633–640.
- Lange OF, et al. (2008) Recognition dynamics up to microseconds revealed from an RDC-derived ubiquitin ensemble in solution. *Science* 320:1471–1475.
- Gerstein M, Lesk AM, Chothia C (1994) Structural mechanisms for domain movements in proteins. *Biochemistry* 33:6739–6749.
- Atilgan AR, et al. (2001) Anisotropy of fluctuation dynamics of proteins with an elastic network model. *Biophys J* 80:505–515.
- Brooks B, Karplus M (1983) Harmonic dynamics of proteins: Normal modes and fluctuations in bovine pancreatic trypsin inhibitor. *Proc Natl Acad Sci USA* 80:6571–6575.
- Levitt M, Sander C, Stern PS (1985) Protein normal-mode dynamics: Trypsin inhibitor, crambin, ribonuclease and lysozyme. *J Mol Biol* 181:423–447.
- Marques O, Sanejouand YH (1995) Hinge-bending motion in citrate synthase arising from normal mode calculations. *Proteins* 23:557–560.
- Ma J, Karplus M (1997) Ligand-induced conformational changes in ras p21: A normal mode and energy minimization analysis. *J Mol Biol* 274:114–131.
- Ma JP, Karplus M (1998) The allosteric mechanism of the chaperonin GroEL: A dynamic analysis. *Proc Natl Acad Sci USA* 95:8502–8507.
- Kabsch W, Sander C (1983) Dictionary of protein secondary structure-pattern-recognition of hydrogen-bonded and geometrical features. *Biopolymers* 22:2577–2637.
- Schlick T, Fogelson A (1992) Tnpack-a Truncated Newton Minimization Package for large-scale problems. 2. Implementation examples. *ACM Trans Math Software* 18:71–111.
- Davis IW, et al. (2007) MolProbity: All-atom contacts and structure validation for proteins and nucleic acids. *Nucleic Acids Res* 35:W375–W383.